

NUMERICAL SIMULATION OF ION THRUSTER OPTICS*

Cody C. Farnell, John D. Williams, and Paul J. Wilbur

Department of Mechanical Engineering
Colorado State University
Fort Collins, CO 80523
Phone: (970) 491-8234
Fax: (970) 491-8671
ccf@engr.colostate.edu

ABSTRACT

A three-dimensional simulation code (ffx) designed to analyze ion thruster optics is described. It is an extension of an earlier code and includes special features like the ability to model a wide range of grid geometries, cusp details, and mis-aligned aperture pairs to name a few. However, the principle reason for advancing the code was in the study of ion optics erosion. Ground based testing of ion thruster optics, essential to the understanding of the processes of grid erosion, can be time consuming and costly. Simulation codes that can accurately predict grid lifetimes and the physical mechanisms of grid erosion can be of great utility in the development of future ion thruster optics designed for more ambitious applications. Results of simulations are presented that describe wear profiles for several standard and non-standard aperture geometries, such as those grid sets with square- or slotted-hole layout patterns. The goal of this paper will be to introduce the methods employed in the ffx code and to briefly demonstrate their use.

THE FFX CODE

Many simulation codes have been developed to study various aspects of ion thruster optics. One such code is the igx code, developed by Nakayama and Wilbur for the high-speed, three-dimensional analysis of grid sets with axially aligned, hexagonal aperture layouts.¹ This code has been shown to agree well with experimental data in high specific impulse applications.² The ffx code analyzes a three-dimensional, rectangular region with symmetry conditions applied on all sides. A uniformly spaced Cartesian mesh, efficient for cell indexing,³ is applied to the volume with each direction having a different mesh spacing. For the simulation of a typical aperture pair in a hexagonal aperture layout, a mesh of approximately 30 by 50 by 300 cells is applied to model two quarter-sized apertures. A cross-section of the typical geometry and applied potentials for a two-grid system is shown in Figure 1.

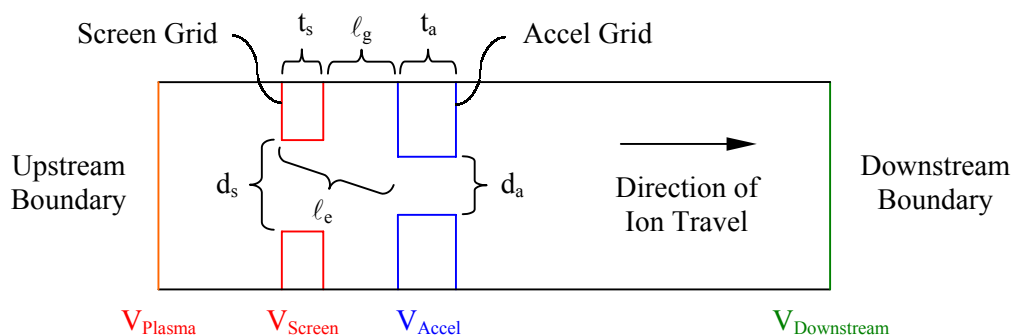


Figure 1. Typical two-grid thruster geometry.

* Presented as paper IEPC-03-073 at the 28th International Electric Propulsion Conference, Toulouse, France, 17-21 March 2003. Copyright © 2003 by the Electric Rocket Propulsion Society. All rights reserved.

The key simulation tasks in the ffx program are outlined in the flowchart in Figure 2. The following discussion will elaborate upon various aspects of these tasks.

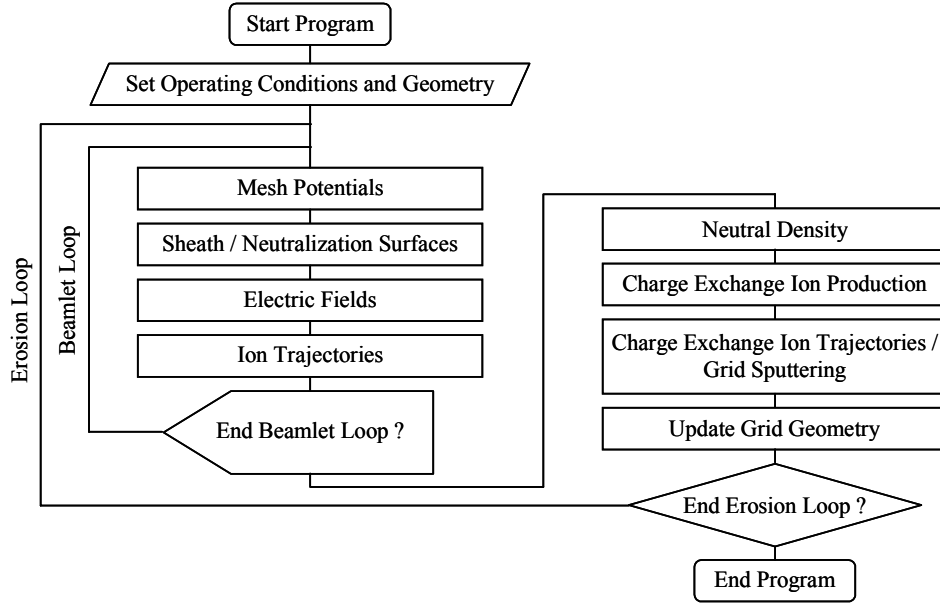


Figure 2. Flowchart of the ffx simulation code.

For the case of an electrostatic thruster, where magnetic fields can be neglected in comparison with the electric fields in the region near the accelerating grids, mesh potential values, denoted by ϕ , are described by the Poisson equation

$$\nabla^2 \phi = -\frac{\rho}{\epsilon_0} \quad \text{or} \quad \frac{\partial^2 \phi}{\partial x^2} + \frac{\partial^2 \phi}{\partial y^2} + \frac{\partial^2 \phi}{\partial z^2} = -\frac{\rho}{\epsilon_0} \quad (1)$$

In this equation, ρ is space charge and ϵ_0 is the permittivity of free space. In the ffx code, both singly and doubly charged ions as well as electrons will contribute to the overall space charge. Thus the right-hand side of this equation will be

$$-\frac{\rho}{\epsilon_0} = -\frac{\rho_+ + \rho_{++} + \rho_e}{\epsilon_0} \quad (2)$$

where ρ_+ and ρ_{++} are the space charge contributions from singly and doubly charged ions respectively, and ρ_e is the space charge contribution from electrons.

Poisson's equation is solved for mesh point potentials at the start of each beamlet loop. Initially, no ion or electron space charge is applied upon the grid mesh. Consequently, the potential solution routine of the code first solves the Laplace equation, where the space charge is zero.

Electric fields in the region are related to potential by

$$\vec{E} = -\nabla \phi \quad \text{or} \quad \vec{E} = -\left(\frac{\partial \phi}{\partial x} \hat{i} + \frac{\partial \phi}{\partial y} \hat{j} + \frac{\partial \phi}{\partial z} \hat{k} \right) \quad (3)$$

The second order partial derivatives in the Poisson equation and the first order partial derivatives in the electric field equation are approximated by finite difference equations of the central difference type.⁴ For instance, in the x direction:

$$\frac{\partial^2 \phi}{\partial x^2} = \frac{-\phi_{i+2} + 16\phi_{i+1} - 30\phi_i + 16\phi_{i-1} - \phi_{i-2}}{12(\Delta x)^2} \quad (4a)$$

$$\frac{\partial \phi}{\partial x} = \frac{-\phi_{i+2} + 8\phi_{i+1} - 8\phi_{i-1} + \phi_{i-2}}{12\Delta x} \quad (4b)$$

Following other simulation codes,^{3,5} equations relating the electron space charge to ion space charge at each mesh point are solved within the potential solution routine of the code depending on the average

upstream and downstream values of space charge and the current value of each mesh potential. In the region upstream of the grids within the discharge chamber plasma:

$$\rho_e = -(\rho_{+0} + \rho_{++0}) \exp\left(\frac{\phi - \phi_0}{T_{e0}}\right) \quad \text{for} \quad \phi \leq \phi_0 \quad (5a)$$

$$\rho_e = -(\rho_{+0} + \rho_{++0}) \cdot \left(1 + \frac{\phi - \phi_0}{T_{e0}}\right) \quad \text{for} \quad \phi > \phi_0 \quad (5b)$$

In the region downstream of the grids within the beam plasma:

$$\rho_e = -(\rho_{+\infty} + \rho_{++\infty}) \exp\left(\frac{\phi - \phi_\infty}{T_{e\infty}}\right) \quad \text{for} \quad \phi \leq \phi_\infty \quad (6a)$$

$$\rho_e = -(\rho_{+\infty} + \rho_{++\infty}) \cdot \left(1 + \frac{\phi - \phi_\infty}{T_{e\infty}}\right) \quad \text{for} \quad \phi > \phi_\infty \quad (6b)$$

In these equations, ϕ_0 is the value of the upstream plasma potential, ϕ_∞ is the value of the downstream plasma potential, ϕ is the current value of the mesh potential, T_{e0} is the upstream electron temperature, and $T_{e\infty}$ is the downstream electron temperature.

The Gauss-Seidel method is used to solve Poisson's equation. In this method, Poisson's equation is rearranged to obtain $\phi_{i,j,k}$ once the finite difference approximations for the partial derivatives have been substituted. Iterations are then performed through all mesh points that are not at a known potential until all of the mesh point potentials are changing by a value less than a preset limit. Relaxation is used to assist convergence of the solution by intuitively predicting each mesh point's next potential value based on the current and last potential values. Relaxation is implemented using

$$\phi_{new} = \alpha \phi_{new} + (1 - \alpha) \phi_{old} \quad \text{where} \quad 0 < \alpha < 2 \quad (7)$$

In this equation, α is called the relaxation parameter. Without the electron density equations embedded within the potential solution, as in the first iteration, using a value for α between 1.0 and 2.0 will increase the rate of convergence, called overrelaxation. With the electron density equations added however, the electron density will change along with mesh potentials during the potential solution, making the solution of the equation non-linear. In this case, a value of α that is between 0.0 and 1.0 is used for convergence, called underrelaxation, because it helps to damp out oscillations that the electron equations create.

Singly and doubly charged ions are represented by particles that are injected into the upstream boundary and terminate upon one of the grids or the downstream boundary. During the movement of these particles, they have the mass and charge of a single ion, whether they are singly or doubly charged. Each of these particles carries with it a much larger charge than a single ion in order to greatly reduce the number of particles required to simulate the ion beamlet. For a typical simulation, about 15,000 particle trajectories are tracked within each beamlet loop. Particles are injected into the upstream boundary of the analysis volume with axial velocities equal to the Bohm velocity:

$$v_{Bohm} = \sqrt{\frac{q \cdot kT_{e0}}{m}} \quad (8)$$

where q is the particle's charge, kT_{e0} is the upstream electron temperature, and m is the mass of the particle.

Forces on charged particles are described by the Lorentz equation:

$$\vec{F} = q(\vec{v} \times \vec{B} + \vec{E}) \quad (9)$$

In this equation, q is particle charge, v is particle velocity, B is the magnetic field, and E is the electric field. In the electrostatic case, again neglecting magnetic field effects, the vector equations governing the motion of particles are given in equations 10a and 10b. The resulting equations of motion in the x direction, for example, are given in equations 11a through 11c.

$$\vec{F} = q\vec{E} = m \frac{d\vec{v}}{dt} \quad (10a) \quad a_x = \frac{qE_x}{m} \quad (11a)$$

$$v'_x = v_x + a_x \Delta t \quad (11b)$$

$$\frac{d\vec{x}}{dt} = \vec{v} \quad (10b) \quad x' = x + v_x \Delta t + \frac{1}{2} a_x \Delta t^2 \quad (11c)$$

The time step Δt is constantly adjusted during particle motion to ensure that a particle's movement is kept under a specified fraction of the smallest mesh spacing, h , in accordance with the Courant condition, i.e.

$$\Delta v \cdot \Delta t \leq \frac{1}{2} h \quad (12)$$

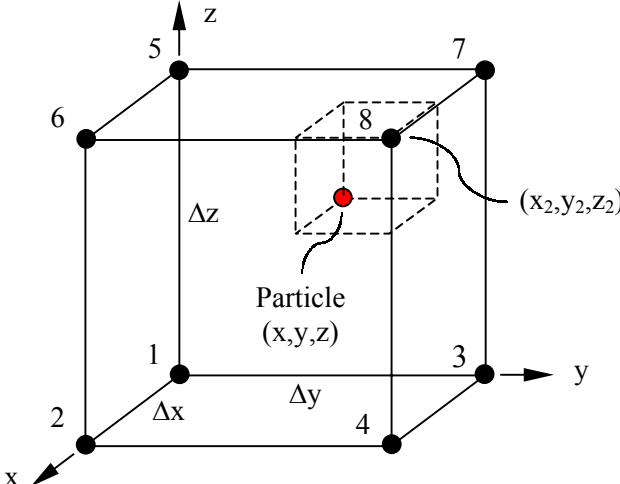
Making sure particles do not travel beyond a certain distance in any given time step is required to ensure that details of the system are not lost.

Throughout particle movement, a particle's total energy remains constant and is given by the sum of its kinetic and potential energies:

$$E = \frac{1}{2} m v^2 + q \phi \quad (13)$$

Using the preceding equations of motion, however, the total energy of a particle is not guaranteed to remain constant. Thus at the conclusion of each time step, its total energy is forced to be constant by adjusting the length of its velocity vector according to the particle's total initial energy and local value of potential. Specifically, the particle's three velocity components are multiplied by the ratio of the required velocity magnitude for energy conservation to its current velocity magnitude in order to maintain the same direction of motion while keeping the total energy of the particle constant.

As particle trajectories are followed through cells, the charge that each particle is carrying is applied to the eight surrounding mesh points by the method of volume weighting. In this method, the charge applied to each mesh point is proportional to the fraction of the total cell volume that the volume closest to the opposite corner occupies. For instance, the charge applied to Point 1 in Figure 3 is proportional to the fraction of the total volume that the volume near Point 8 occupies:



$$chg_{\text{Point 1}} = chg_{\text{Particle}} \cdot \frac{(x_2 - x) \cdot (y_2 - y) \cdot (z_2 - z)}{\Delta x \cdot \Delta y \cdot \Delta z} \quad (14)$$

Figure 3. Method of volume weighting.

During particle movement, the electric fields in each direction at the particle's actual location are interpolated from the known electric fields at the eight corner mesh points of the cell using the same weighting scheme that is used to apply charges onto the mesh points in a reverse manner. The electric field at the particle in the x direction, for example, is the sum of the eight x direction electric fields at the corner points multiplied by the eight respective volume fractions.

The neutral density in each cell, n_n , is calculated by assuming a radially uniform, free molecular flow of neutral particles. Clausing factors, which are dependent on each grid's thickness and aperture area, are used to adjust the neutral density through the grids. An upstream neutral density can be specified, or the beamlet current and propellant utilization efficiency can be used to determine the flow rate through the region.

Once singly and doubly charged ion densities and the neutral density in each cell have been calculated, equations describing the volumetric charge exchange ion production rates in each cell are used to introduce charge exchange ions. Charge exchange ions are created when electrons from fast moving ions

transfer to relatively slow moving neutral atoms, creating slowly moving ions and fast moving neutral atoms. Charge exchange ion production rates are described using equations of the form

$$\frac{dn_{cx}}{dt} = n_n n_i v_i \sigma(v_i) \quad (15)$$

Depending on the reaction in question, n_i can be the singly or doubly charged ion density, v_i the velocity that a singly or doubly charged ion would be moving through the cell, and $\sigma(v_i)$ the cross section of the specific reaction.

Erosion of the grids can be due to both ions from the upstream plasma as well as charge exchange ions impacting the grids. The number of sputtered grid atoms is dependent on the energy and angle of incidence of the impacting particle. The angle of incidence is found using the local surface normal vector of the impacted cell. Because erosion will constantly change the grid surface, surface normal vectors are found at any time by calculating the location of the regional center of mass of the impacted cell relative to its geometrical center. The surface normal of the impacted cell is then defined as the line that extends from the center of mass in the region through the center of the impacted cell, as shown in Figure 4.

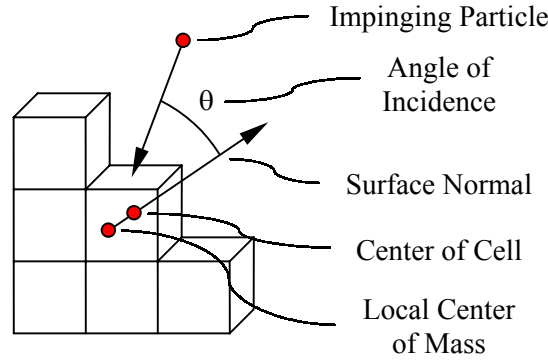


Figure 4. Surface normal vectors and angle of incidence.

Grid atoms are sputtered with a cosine distribution based on the surface normal vector of the impacted cell and are subsequently followed from the particle impact point until they deposit onto one of the grids or exit through the upstream or downstream boundaries.

Charge exchange ions originating from several centimeters downstream of the grids can flow back to the accel grid and cause erosion. To keep an analysis volume of reasonable size and a simulation of reasonable speed while still simulating charge exchange ions from far downstream, charge exchange ion production is adjusted near the downstream boundary to bring the current reaching the accel grid to the desired level.

RESULTS

To illustrate the use of the ffx code, simulations were run on four SUNSTAR (Scaled Up NSTAR) grid sets that have various aperture patterns. The geometries of these grids and the simulated operating conditions are shown in Figure 5. The parameter chosen to compare the grid sets is normalized perveance per unit grid area:

$$P_{TG} = \frac{\left(\frac{J_b}{A_{TG}}\right) \frac{l_e^2}{V_T^{3/2}}}{\frac{4\epsilon_0}{9} \sqrt{\frac{2e}{m}}} \quad \text{where} \quad l_e = \sqrt{(t_s + l_g)^2 + \frac{d_s^2}{4}} \quad (16)$$

In these equations, J_b is the beamlet current, A_{TG} the aperture and web area, l_e the effective grid spacing, and V_T the total accelerating voltage. A comparison of the beamlet shapes at the perveance and crossover impingement limits is shown in Figure 6. At the perveance limit, where extraction currents are relatively high, ions impinge upon the accel grid on the same side of the aperture from which they started. At the crossover limit, where extraction currents are relatively low, ions can crossover the aperture centerline and impinge upon the opposite side of the accel grid. At the center of a thruster, aperture pairs would likely be

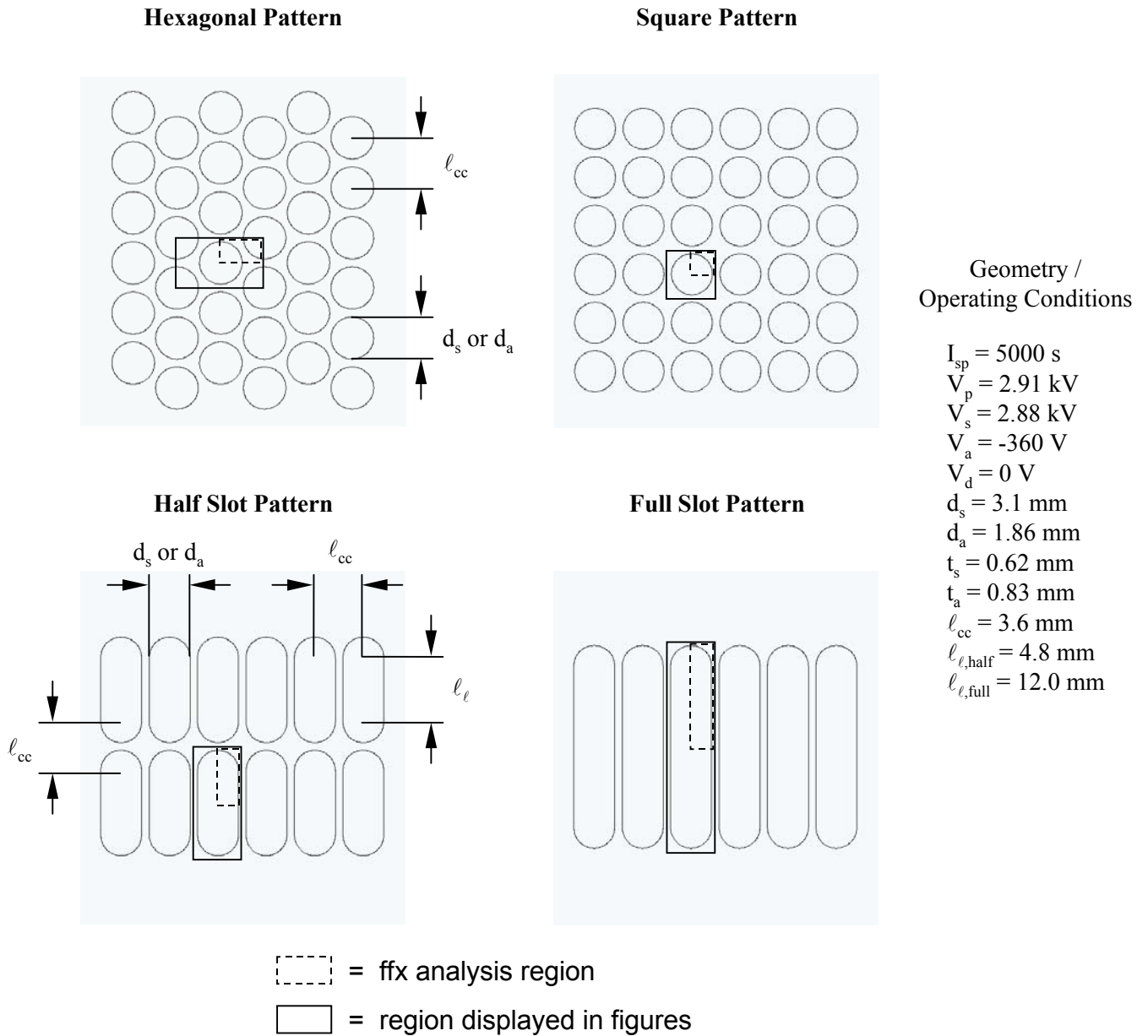


Figure 5. SUNSTAR grid aperture patterns.

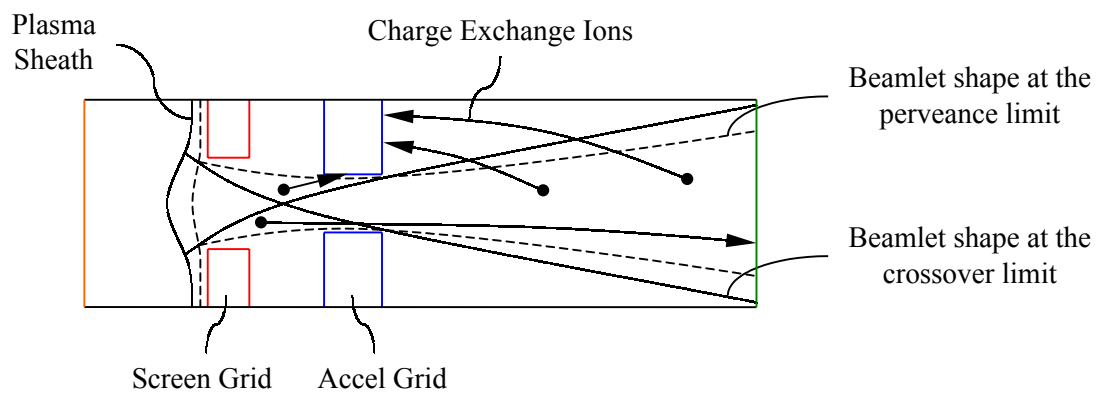


Figure 6. Perveance and crossover impingement limits.

operating closer to the perveance limit where ion densities are high. Conversely, at the edges of the thruster, aperture pairs would be operating closer to the crossover limit where ion densities are lower.

Figure 7 compares the impingement limits found experimentally at CSU⁶ with those found using the ffx code for the four SUNSTAR aperture patterns. The ffx code generally predicted slightly greater perveance and crossover limits than those found experimentally. Overall, good agreement was seen between the relative limits among different aperture patterns.

Figure 8 compares the sheath and neutralization surface shapes found near the perveance and crossover limits for each of the aperture patterns. The sheath and neutralization surfaces shown here are surfaces of constant potential: the sheath at the upstream plasma potential and the neutralization surface at the downstream plasma potential.

Erosion tests were run on the four SUNSTAR grid sets at beamlet current values near the perveance limit for each grid set. In each case, the current reaching the accel grid was adjusted to 0.3% of the beamlet current. Figure 9 compares the erosion patterns produced on each of the grid sets at two values of propellant throughput, the second being twice as much as the first. Note that each of the grid sets would be run for different amounts of time to reach the same level of propellant throughput. Because the grids are operating near the perveance limit, high-energy charge exchange ions produced in the region between the grids quickly erode away the accel grid barrel from the upstream side of the accel grid in all of the aperture layouts. Following this period of immediate barrel erosion, charge exchange ions from the downstream region create erosion patterns in the downstream side of the accel grid with less accel grid barrel erosion. The familiar pit and groove pattern of erosion can be seen for the hexagonal aperture pattern.

CONCLUSIONS

A three-dimensional optics simulation code was developed that can be used to simulate ion optical behavior in complex grid geometries with reasonable efficiency. Results from the code were found to be consistent with experimental data in predicting impingement limits. Erosion patterns predicted by the code agree well with the known erosion patterns of grids with hexagonal aperture layouts, and the code yields erosion patterns for grids with square and slotted aperture layouts that are judged to be reasonable.

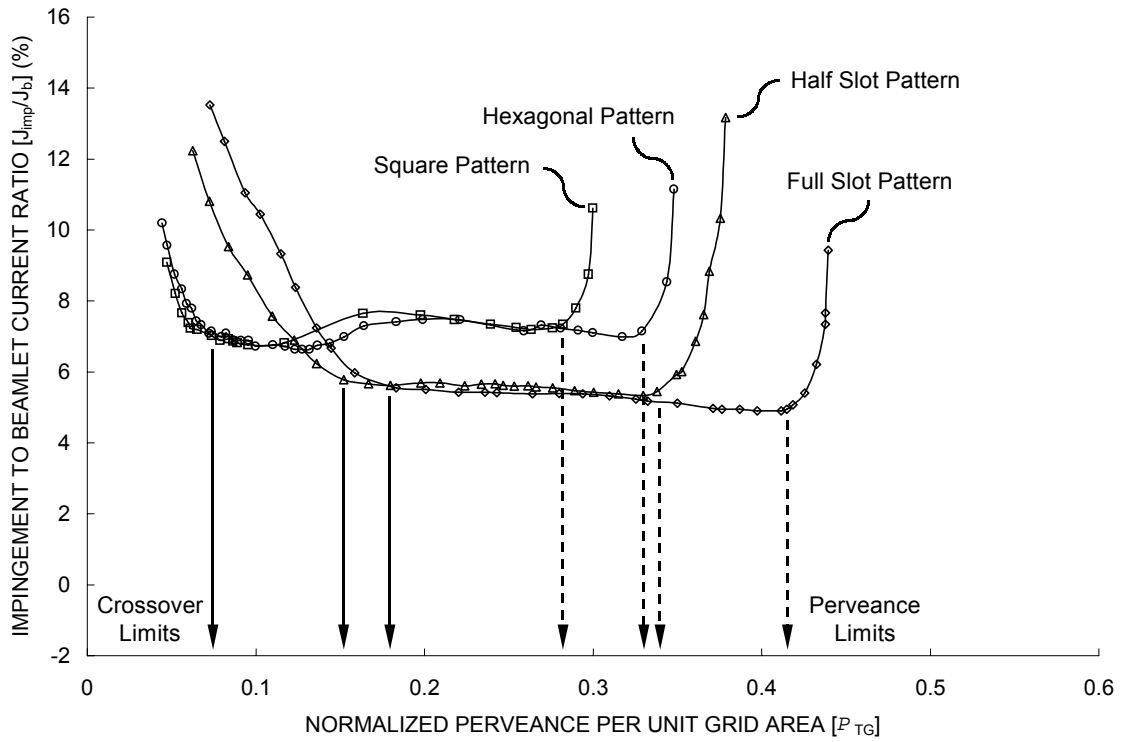
ACKNOWLEDGMENT

Financial support provided in part by the ion propulsion program at the NASA Glenn Research Center is gratefully acknowledged.

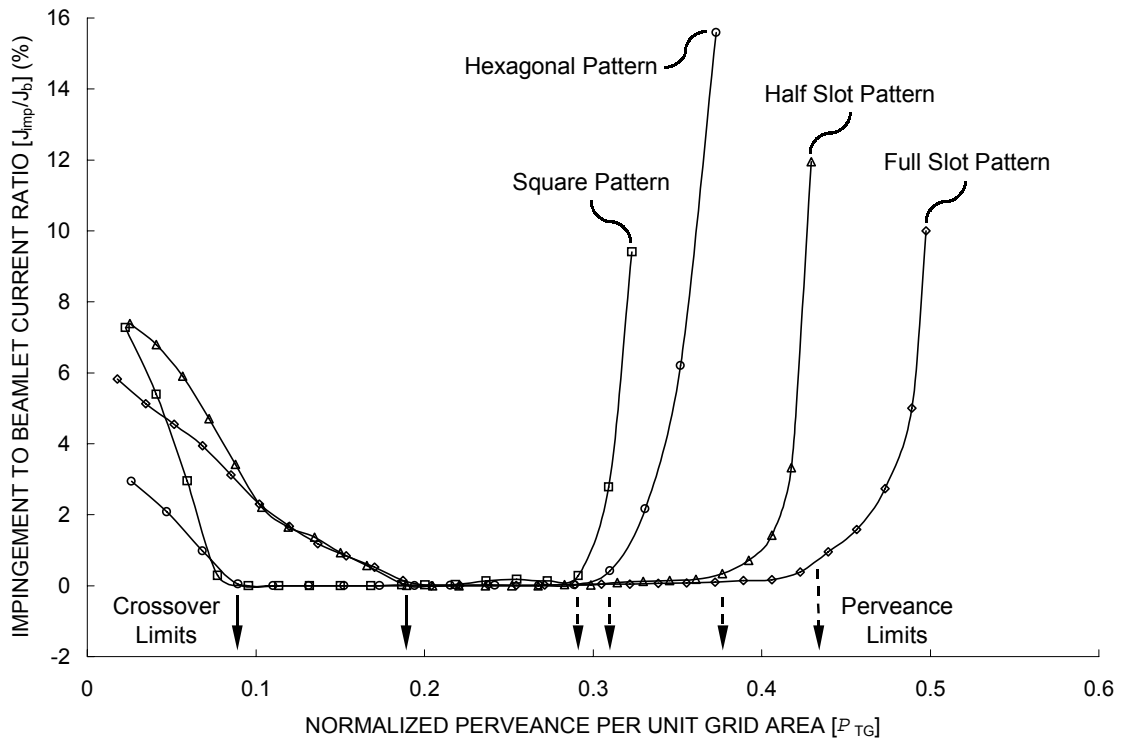
REFERENCES

- ¹ Nakayama, Y. and Wilbur, P. J. "Numerical Simulation of High Specific Impulse Ion Thruster Optics." 27th International Electric Propulsion Conference, IEPC-01-099, Pasadena, CA, October 2001.
- ² Wilbur, P. J., Miller, J., Farnell, C., and Rawlin, V. K. "A Study of High Specific Impulse Ion Thruster Optics" 27th International Electric Propulsion Conference, IEPC-01-098, Pasadena, CA, October 2001.
- ³ Wang, J., Polk, J. "Three-Dimensional Particle Simulations of Ion Optics Plasma Flow and Grid Erosion." 33rd Plasmadynamics and Lasers Conference, AIAA 2002-2193, Maui, Hawaii, May 2002.
- ⁴ Chapra, S. C., and Canale, R. P. *Numerical methods for engineers*, 3d ed., McGraw-Hill, New York, 1998.
- ⁵ Brown, Ian. *The physics and technology of ion sources*, John Wiley & Sons, New York, 1989.
- ⁶ Williams, J. D., Monthly Report to the Jet Propulsion Laboratory, December 18, 2002. See also in this conference J.D. Williams, D.M. Laufer, and P.J. Wilbur, "Experimental Performance Limits on High Specific Impulse Ion Optics," 28th International Electric Propulsion Conference, IEPC-03-128, Toulouse, France, 17-21 March 2003.

Experimental



ffx Code



Note: Charge exchange impingement current was not included in the ffx data.

Figure 7. Comparison of experimental and ffx code predictions of crossover and perveance limits.

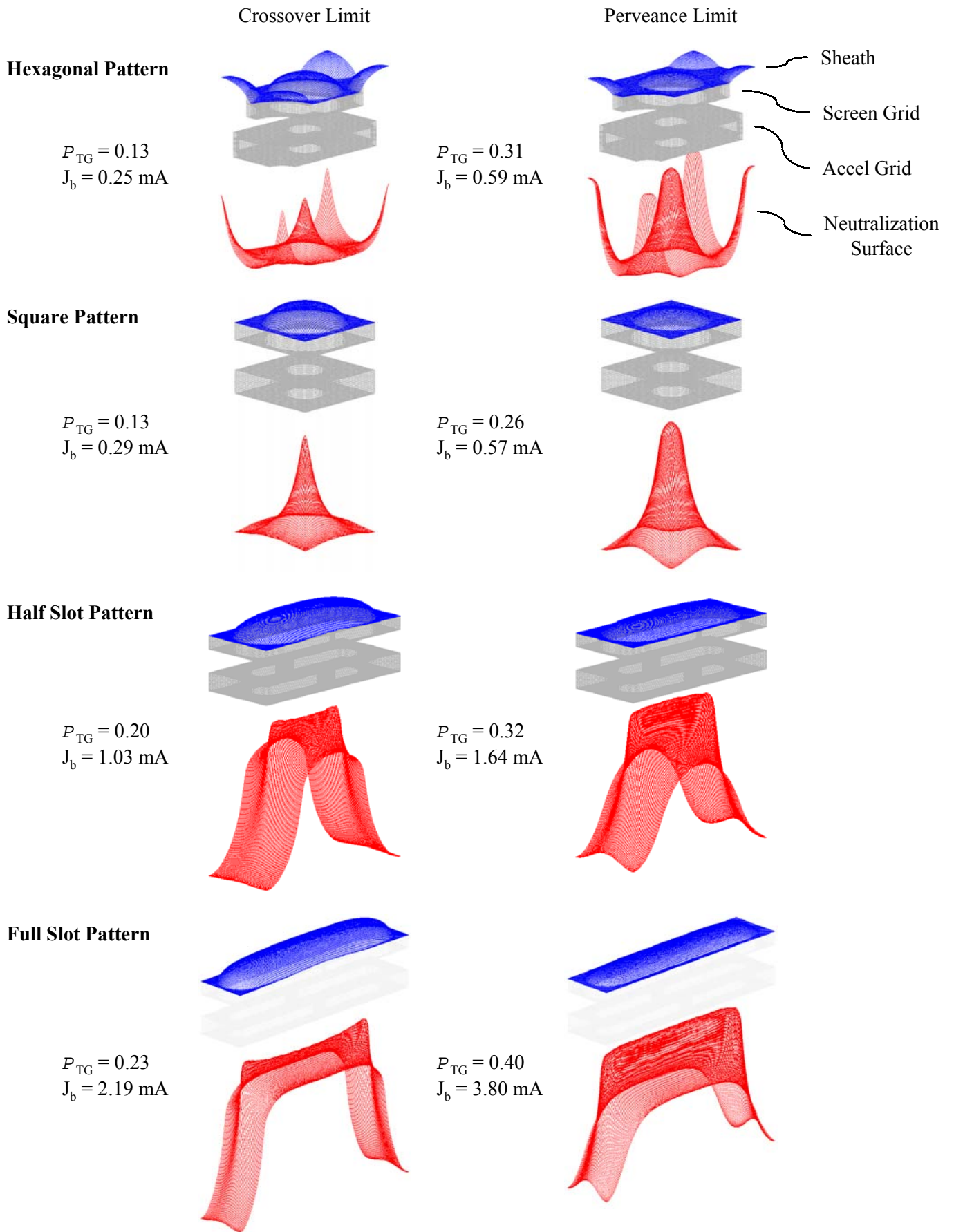


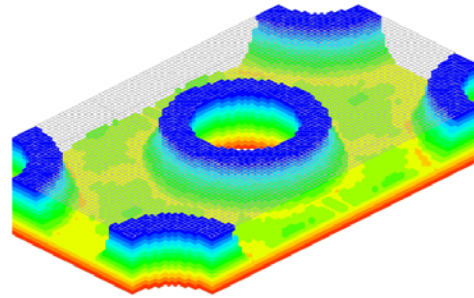
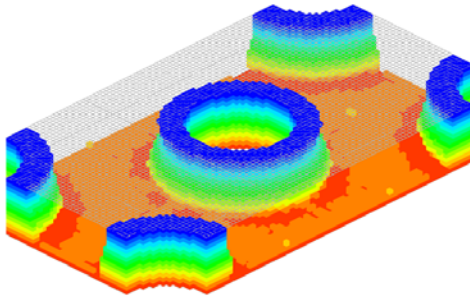
Figure 8. Sheath and neutralization surface shapes for the four SUNSTAR grid sets.

Propellant Usage 1
 (~5000 hours of operation
 for hexagonal grid)

Propellant Usage 2
 (~10000 hours of operation
 for hexagonal grid)

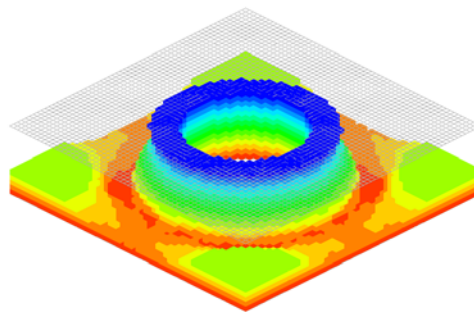
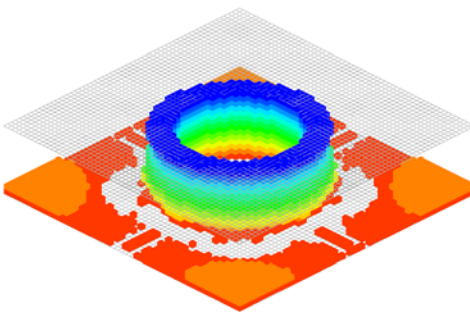
Hexagonal Pattern

$P_{TG} = 0.31$
 $J_b = 0.59 \text{ mA}$



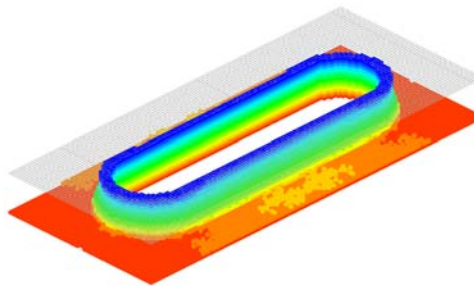
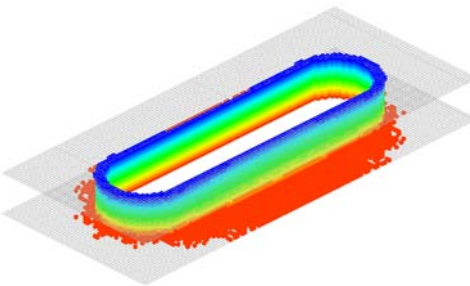
Square Pattern

$P_{TG} = 0.26$
 $J_b = 0.57 \text{ mA}$



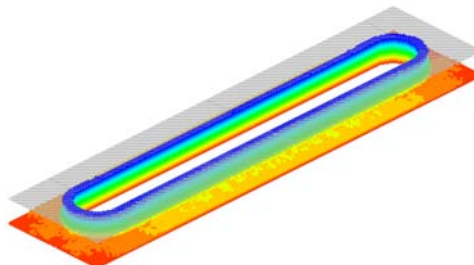
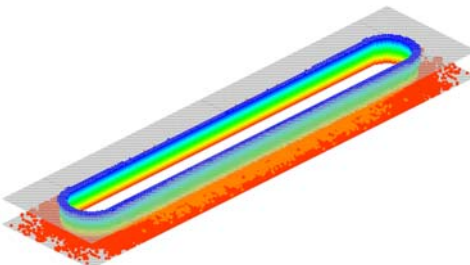
Half Slot Pattern

$P_{TG} = 0.32$
 $J_b = 1.64 \text{ mA}$



Full Slot Pattern

$P_{TG} = 0.40$
 $J_b = 3.80 \text{ mA}$



Upstream
Cells



Downstream
Cells

Note: Colored cells are cells that have been eroded away.

Figure 9. Accel grid cell erosion for the four SUNSTAR grid sets.